

# A Measurement of the Attenuation of Drifting Electrons in the MicroBooNE LArTPC

The MicroBooNE Collaboration

August 30, 2017

## Abstract

MicroBooNE, an 85-ton active mass liquid-argon time-projection chamber (LArTPC) detector located on the Fermilab's Booster Neutrino Beamline (BNB), is designed to both probe neutrino physics phenomena and further develop the LArTPC detector technology. MicroBooNE, the largest currently operating LArTPC detector in the world, began collecting data in fall 2015. The exceptional imaging capabilities of LArTPCs allow unprecedented study of neutrino interactions. A fundamental requirement for the performance of such detectors is to maintain electronegative contaminants such as oxygen and water at extremely low concentrations, which otherwise can capture the ionization electrons. This note presents a first measurement of the electron attenuation as a function of drift time, using cosmic ray muon data collected by MicroBooNE. The observed electron attenuation indicates that during stable purity period, the lowest electron drift-lifetime observed is 18.0 ms which corresponds to a charge loss of 12% over the full drift distance at an electric field of 0.273 kV/cm and an O<sub>2</sub> equivalent contamination of 17 ppt. This is an indication that the argon purification and recirculation system of MicroBooNE is performing successfully.

# Contents

<b>1</b>	<b>Introduction</b>	<b>3</b>
<b>2</b>	<b>The MicroBooNE LArTPC</b>	<b>5</b>
<b>3</b>	<b>Event samples</b>	<b>6</b>
<b>4</b>	<b>Reconstruction</b>	<b>7</b>
4.1	Reconstructing the arrival times of cosmic-ray tracks . . . . .	8
<b>5</b>	<b>Event selection</b>	<b>8</b>
<b>6</b>	<b>Extracting charge dependency from drift time</b>	<b>9</b>
6.1	Space charge in liquid argon . . . . .	11
6.1.1	Effect of space charge on $dQ/dx$ . . . . .	13
6.1.2	Space charge corrections . . . . .	14
6.2	Comparison between Data and Simulation . . . . .	16
<b>7</b>	<b>Location dependence of <math>Q_A/Q_C</math></b>	<b>19</b>
<b>8</b>	<b>Systematic uncertainties</b>	<b>21</b>
8.1	Space charge correction . . . . .	21
8.2	Recombination model . . . . .	22
8.3	Diffusion . . . . .	22
8.4	Systematics summary . . . . .	24
<b>9</b>	<b>Results</b>	<b>25</b>
<b>10</b>	<b>Future plans</b>	<b>25</b>
<b>11</b>	<b>Summary and conclusions</b>	<b>26</b>

# 1 Introduction

Liquid argon time projection chambers (LArTPCs) are imaging detectors that offer exceptional calorimetric and position resolution capabilities for studying particle interactions in argon. They are currently the most favored technology for current and future neutrino experiments. A LArTPC consists of a cathode plane and finely segmented (mm-scale) anode planes enclosed in a volume of highly purified liquid argon. Neutrino or cosmic interactions with liquid argon in the TPC produce charged particles that cause ionization and excitation of argon. An electric field drifts ionization electrons towards finely segmented anode wire planes oriented at different angles to provide stereoscopic views of the interaction. The excitation of argon produces prompt scintillation light giving important timing information about the neutrino interaction. Knowledge of the electron drift velocity, combined with timing information, and signals on multiple wire planes, allow a three dimensional image of the interaction to be produced.

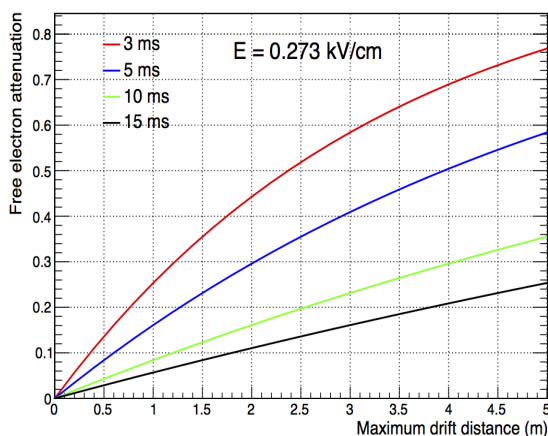


Figure 1: Drift electron attenuation as a function of maximum drift path (in m) for an electric field of 0.273 kV/cm. The colored curves correspond to different values of the detector parameter, electron drift-lifetime ( $\tau$ ). In 100% pure liquid argon, electrons will drift forever resulting in infinite lifetime.

One of the important operational requirements of a LArTPC is to keep electronegative impurities such as oxygen and water at extremely low concentrations. These contaminants<sup>1</sup> capture the drifting ionization electrons (signal) and thereby reduce the size of the recorded TPC signals. This can affect both energy measurements and track reconstruction, particularly for events far from the anode wires. The electron lifetime is inversely proportional to the impurity concentration [1, 2] and hence provides a direct measurement of the liquid argon impurity content. As an example, Figure 1 shows the drift-electron attenuation as a function of maximum drift path for a uniform electric field of 0.273 kV/cm and a drift velocity of 114 cm/ms for different electron drift-lifetimes. To achieve less than 36% signal loss for a drift distance of 2.56 m (equivalent to a 5-ms lifetime in an electric field of 0.273 kV/cm), the O<sub>2</sub> equivalent contamination is required to be as low as 60 parts per trillion (ppt). Similarly, to achieve a signal loss of less than 20% (or a lifetime of 10 ms at 0.273 kV/cm), the O<sub>2</sub> equivalent concentration is required to be less than 30 ppt. Commercial liquid argon typically contains parts per million (ppm) oxygen concentration levels. Liquid argon can also become contaminated inside the cryostat due to the out-gassing of the warm walls, cables and other TPC components present in the gaseous argon volume. Additionally, virtual leaks (such as from the parts located close to the feedthroughs) can also become a constant source of impurities. The desired purity is therefore achieved using a continuous liquid-argon recirculation

<sup>1</sup>Another impurity of concern is nitrogen (N<sub>2</sub>) which can quench as well as absorb the scintillation light produced in neutrino-argon interactions. The concentration of N<sub>2</sub> is required to be less than 2 parts per million (ppm). But, liquid argon cannot be efficiently purified for N<sub>2</sub>, hence the required low contamination level for N<sub>2</sub> has to come from the manufacturer. Note that even multi-ppm levels of nitrogen do not affect the ionization charge.

system and dedicated filters to remove oxygen and water.

In general, the level of purity inside a liquid argon volume can be measured in four ways: a) using gas analyzers [3] b) using purity monitors [3, 4], c) using laser tracks [5], and d) using long minimum-ionizing cosmic-ray muon tracks [6]. This note will only discuss the measurement of liquid argon purity using cosmic-ray muon tracks in the MicroBooNE detector. As MicroBooNE is located only a few meters below the surface, a large flux of cosmic-ray muons enter the detector volume. Using long tracks from minimum ionizing particles, such as cosmic ray muons, to determine the drift-electron lifetime has several advantages over the other techniques. For example, the use of purity monitors has practical advantages in terms of speed of measurement and the ability to measure low electron drift-lifetimes before tracks can be reconstructed. The technique of using tracks has the statistical and systematic advantage that one can use the charge information over the full range of electron drift-times on each track to measure the electron drift-lifetime thereby allowing for internal consistency checks and the measurement of long electron drift-lifetimes. If there is indeed a variation of the electron drift-lifetime over the cryostat volume, the tracks (if they are distributed uniformly) will give an appropriate average value for electron drift-lifetime while a purity monitor gives the value in one location. Tracks also have the potentially important systematic advantage that one is measuring the effect of the contaminants at the relevant electric field while the purity monitor typically measures the effect of the contaminants at a lower electric field. In fields above about 200 V/cm, the drift-field increases the speed of the drift electrons and this can lead to a different electron capture cross section on the contaminants for the purity monitor and the drift-electrons in the TPC.

## 2 The MicroBooNE LArTPC

MicroBooNE [7, 8] is an 85-ton active volume LArTPC neutrino experiment located on the Fermilab Booster Neutrino Beamline (BNB). MicroBooNE is an important step towards LArTPC R&D in establishing large-scale detectors for neutrino physics. MicroBooNE brings two main technological advances including argon purification without evacuation. They are cold (in argon) front-end electronics and a large (2.56 m) electron drift. The two main physics goals of MicroBooNE are the investigation of the low-energy excess of electron neutrino-like events seen previously by MiniBooNE [9, 10] and precision measurements of  $\nu$ -Ar interactions in the 1 GeV range. The purification of liquid argon in MicroBooNE is achieved by two pairs of filters, with each pair consisting of two filter vessels, one for filtering water and the other for oxygen. The water filter vessels are filled with 4Å molecular sieves supplied by Sigma-Aldrich [11]. The oxygen filter vessels are filled with BASF CU-0226 S, a dispersed copper oxide impregnated on a high surface area alumina [12]. The MicroBooNE argon recirculation system is designed to extract argon in two places and sent back into the cryostat from a single port. Liquid argon is extracted from the bottom upstream end of the cryostat whereas the gaseous argon from the very top of the cryostat is condensed and extracted from the cryostat. Argon from both of these paths is sent to the purification system. The clean argon that enters the cryostat from the top downstream end is brought to the bottom of the cryostat via a pipe that lies within the cryostat.

A layout of the MicroBooNE detector is shown in Figure 2 (left). In MicroBooNE, the distance between the cathode and anode is 2.56 m. The cathode is at a voltage of -70 kV which results in a drift field of 0.273 kV/cm. At this electric field, an ionization electron takes about 2.2 ms (with a drift velocity of 114 cm/ms) to travel the full drift distance. The anode region consists of three wire planes with a total of 8256 wires. The collection plane ( $W$ ) is vertical, the two induction planes ( $U$  and  $V$ ) are oriented at an angle of  $60^\circ$  with respect to the vertical. The MicroBooNE coordinate system is shown in Figure 2 (right). The spacing between consecutive wires and wire planes is 3 mm. The first induction plane is biased at -110 V and the collection plane is biased at +230 V with respect to the middle wire plane. These bias settings allow the wire planes to be transparent to drifting electrons. The nominal electronics gain and shaping time are 14 mV/fC and 2  $\mu$ s, respectively. The MicroBooNE light collection system consists of 32 8-inch photo-multiplier tubes (PMTs) that are located just behind the wire planes and detect scintillation light. A recorded event in MicroBooNE has a duration of 4.8 ms with a digitization frequency of 2 MHz. MicroBooNE finished commissioning in summer 2015 and has been taking

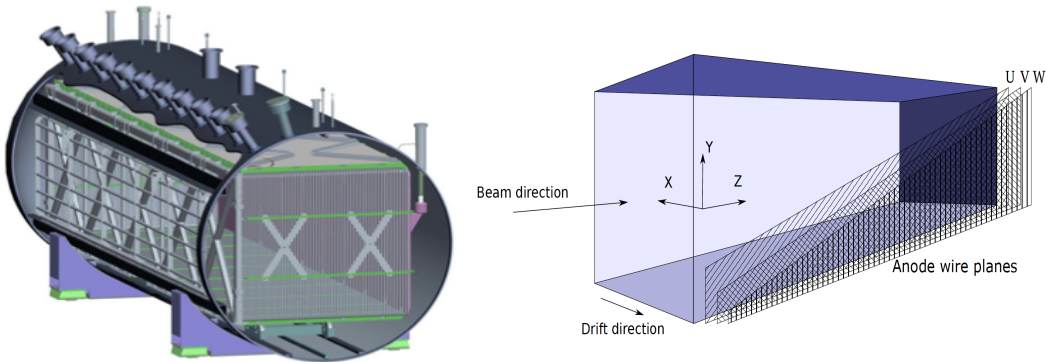


Figure 2: (left) Layout of the MicroBooNE experiment. The MicroBooNE TPC is about 10.4 m long, 2.3 m high, and 2.5 m wide. (right) The MicroBooNE coordinate system. The three wire planes are vertical (collection plane, W) and at  $\pm 60^\circ$  to the vertical (induction planes, U and V).

cosmic-ray (Booster Neutrino Beam) data since August (October) 2015.

### 3 Event samples

Cosmic-ray muon data taken between 02/16/2016 and 04/21/2016 are used for this analysis. LArSoft [13] was used to reconstruct the data. Approximately 5000 total events per day of data-taking were processed in order to study the variation in electron lifetime on a daily basis during the time period 02/16/2016 – 04/21/2016. Data corresponding to 03/05/2016 and 03/17/2016 – 03/25/2016 are not included in the analysis due to problems in processing the data. Also, the datasets were chosen such that there is approximately 24 hour difference in time between consecutive runs.

The data during the selected run period include both high- and low-purity conditions. On 03/02/2016, the liquid argon circulation pump tripped as a result of oxygen deficiency hazard (ODH) system test resulting in a drop of lifetime from 9 ms to 5 ms according to the purity monitor data. On 03/04/2016, due to power outage from 10 a.m. to midnight, lower lifetime was recorded. During 03/29/2016 – 03/31/2016, the electron lifetime dropped due to liquid argon top-off<sup>2</sup>.

Monte Carlo (MC) simulation samples were also used in this analysis for systematic error studies. All the simulation samples used in this analysis are single muons generated isotropically in the detector with start positions at the center of the TPC ( $X=128.0$  cm,  $Y=0.0$  cm, and  $Z=518.5$  cm). The muon momentum ranges from 0 to 2.0 GeV. The muon angle with respect to the  $X$ - $Z$  plane ranges from  $0^\circ$  to  $180^\circ$  and the angle with respect to the  $Y$ - $Z$  plane ranges from  $0^\circ$  to  $90^\circ$ . The same reconstruction chain used in data was also used in simulation.

### 4 Reconstruction

The raw signal recorded on the wires first passes a noise filter [14], before hits (ionization signals) are extracted from the observed waveforms on each wire. Reconstructed hits that are connected in space and time are then grouped into clusters. Clusters are merged between planes based on temporal and spatial information in order to create three-dimensional reconstructed objects (tracks and showers). The calorimetric reconstruction [15, 16] of tracks starts by converting the hit amplitude (in units of ADC counts) to charge (in units of electrons) using an electronics calibration factor. In the next step, a correction is made for ionization charge loss along the drift due to electron-negative impurities in liquid argon. This measured charge,  $dQ$ , is then normalized

<sup>2</sup>The gas analyzers [3] constantly draw a small amount of gas from the cryostat so periodically argon gas is sent from the dewar to the condenser to maintain argon levels in the cryostat. This procedure is called liquid argon top-off.

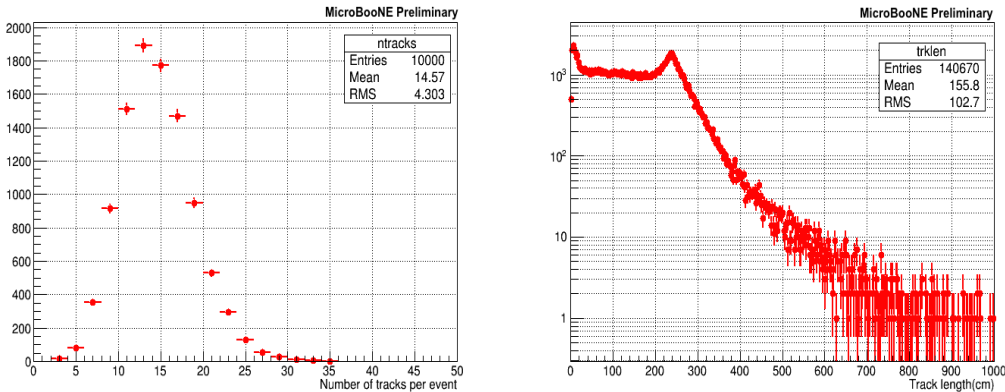


Figure 3: (left) Distribution of the number of reconstructed tracks per event (for full read-out window) using a cosmic-ray data sample containing 10,000 cosmic-ray events (data runs 5411 and 5600). (right) 3D reconstructed track length distribution of all the tracks in the data sample.

for the track pitch length ( $dx$ ) to obtain the charge deposited per unit track length,  $dQ/dx$ . Finally,  $dQ/dx$  is converted to energy released per unit track length,  $dE/dx$ , by accounting for ionization charge loss due to argon-ion recombination process using the modified-box model [16].

Figure 3 shows example distributions of the average number of cosmic-ray tracks per event (left) and corresponding 3D reconstructed track length distributions (right) using a cosmic-ray data sample before any event selection is applied. On an average, about 15 cosmic-ray muons enter the TPC active volume per recorded event (Figure 3, left).

#### 4.1 Reconstructing the arrival times of cosmic-ray tracks

Since hits are treated independently from tracks in this analysis, we need to know how far the electrons associated with each hit drifted before arriving at the collection-plane. This is equivalent to knowing  $t_0$ , the time that the muon traversed the chamber. One can extract the  $t_0$  information by associating reconstructed TPC objects with the corresponding scintillation light objects recorded in the system of PMTs. At the time of this analysis, the light reconstruction of PMT data in MicroBooNE is not reliable for  $t_0$  extraction. Here we use cosmic-ray muon tracks that cross both anode and cathode instead which does not require PMT information. For these crossing tracks,  $t_0$  is associated with the minimum hit  $X$  (drift) coordinate. As one might expect, crossing tracks are rare, with only about three tracks in a 100 event sample.

### 5 Event selection

A series of selection cuts as listed below are applied to data to select a crossing track cosmic-muon sample.

- **Require that the track length projected onto the  $X$  (drift) direction is between 250 cm and 270 cm.** Crossing tracks are expected to have a sharp peak at 256 cm. A spread of a few centimeters around this value is observed in the data. The spread is likely due to spatial distortions caused by space charge effects [17]. Figure 4 (left) shows an example track length distribution in the drift direction using a cosmic-ray data sample containing 10,000 events. The highlighted region shows the selected crossing track band.
- **Exclude tracks with  $75^\circ < \theta_{XZ} < 105^\circ$  and  $85^\circ < \theta_{YZ} < 95^\circ$ .**  $\theta_{XZ}$  is the angle with respect to the  $X$ - $Z$  plane and is defined as the inverse of the tangent of the ratio of track start in  $X$  and  $Z$  directions, where track start represents the vertex direction.  $\theta_{YZ}$  is the angle with respect to the  $Y$ - $Z$  plane and is defined as the inverse of the tangent of the ratio of track start in  $Y$  and  $Z$  directions. Figure 5 shows an illustration of these

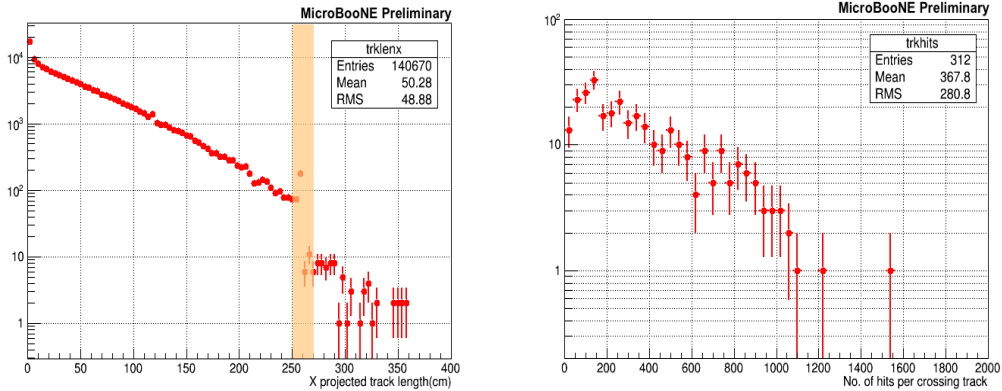


Figure 4: (left) Distribution of the  $X$ -projected track length distribution using 10,000 events from cosmic-ray data (runs 5411 and 5600). The highlighted band shows the region used to select anode-cathode crossing tracks. (right) Distribution of number of hits per crossing track for the sample used in the left plot.

Applied cut	Number of tracks left	Percentage drop (%)
No cut	731093	
Crossing track	1652	99.8
Reject tracks with: $75^\circ < \text{abs}(\theta_{XZ}) < 105^\circ$ , or $85^\circ < \text{abs}(\theta_{YZ}) < 95^\circ$	1180	28.6
Number of track hits > 100	1142	3.2

Table 1: Impact of each applied cut on the track statistics for a cosmic-ray data sample consisting of 50,000 events.

angles in the MicroBooNE coordinate system. The  $\theta_{XZ}$  ( $\theta_{YZ}$ ) cut eliminates tracks that are nearly perpendicular (parallel) to the collection plane wires. These tracks are difficult to reconstruct, and thus lower the quality of calorimetric reconstruction. Figure 6 shows  $dQ/dx$  of hits as a function of  $\theta_{XZ}$  and  $\theta_{YZ}$  angles before any angular cuts are applied.

- **Require that each selected crossing track contains at least 100 hits in the collection plane.** This ensures uniform density of hits along the drift direction. Figure 4 (right) shows an example distribution of number of hits per crossing track before any selection cuts using a cosmic-ray data sample containing 10,000 events. Table 1 shows the effect of each applied cut, listed so far, on track statistics using a cosmic-ray data sample of 50,000 events.
- **Exclude TPC regions associated with shorted channels.** Require that the hit  $Z$  and  $Y$  coordinates are in a region of the TPC that does not correspond to shorted channels [14]: ( $250 < Z < 675$ ) cm and ( $-100 < Y < 20$ ) cm. In the other regions of the TPC, the collection plane response is altered due to shorted channels, affecting the  $dQ/dx$  reconstruction. Since we know that the regions of modified response are not yet being properly reconstructed, we chose to exclude them from the analysis. Initial observations showed that this cut improves the  $dQ/dx$  reconstruction near the anode. Note that in the case of simulation, one usually does not require this cut as shorted channels are not implemented in MC simulation. However, we apply this cut for simulation samples with space charge and recombination simulation since space charge effect is a 3D effect and will result in position dependence.

We fit to the Landau peak of the hit  $dQ/dx$  distribution to extract  $dQ/dx$  relative to the MIP value in a given drift bin (see Section 6 for more details on the analysis method). Therefore, no explicit cuts are required to remove high-charge hits such as those produced by delta rays.

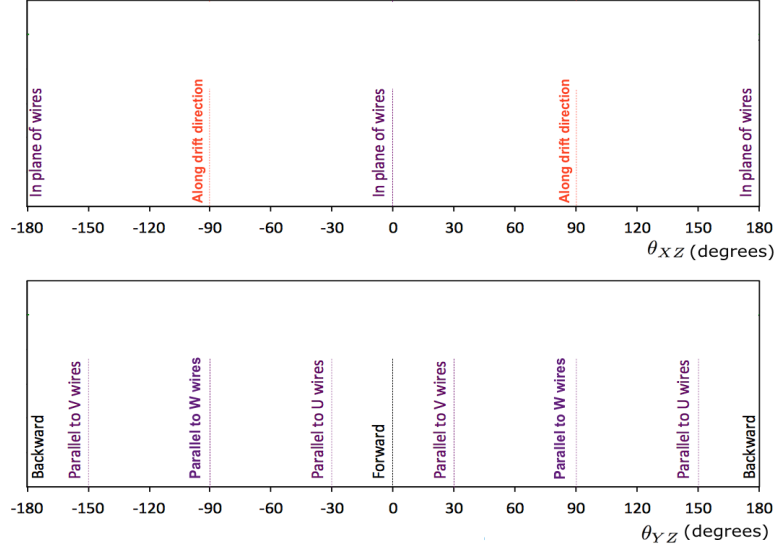


Figure 5: (top) Definition of various  $\theta_{XZ}$  angles. (bottom) Definition of various  $\theta_{YZ}$  angles.

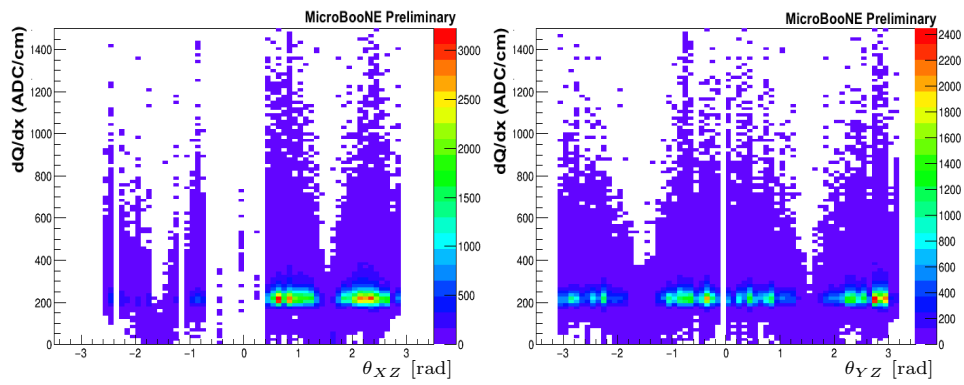


Figure 6:  $dQ/dx$  distribution as a function of angles  $\theta_{XZ}$  (left) and  $\theta_{YZ}$  (right) for crossing tracks before applying any angular cuts. The plots are made using a 20,000 event cosmic-ray data sample.

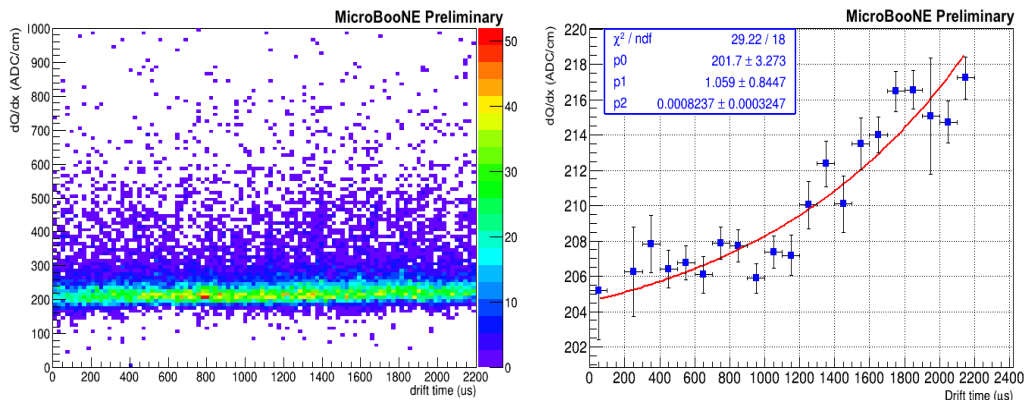


Figure 7: (left)  $dQ/dx$  vs drift time scatter plot for Run 5411 using the event selection described in Section 5. (right) The most probable value for  $dQ/dx$  extracted from Landau convolved Gaussian fits to each drift bin (see Figure 8) plotted as a function of drift time. In the example shown, an exponential plus constant function is used to fit the points.

## 6 Extracting charge dependency from drift time

All collection plane hits associated with the tracks passing the selection are used. Each track-hit  $X$  position is corrected for the track  $t_0$ . The resulting  $dQ/dx$  on the collection plane wires for all tracks is plotted as a function of (corrected) drift time as shown in Figure 7 (left). The  $dQ/dx$  distribution is then split into 22 drift time bins of 100  $\mu\text{s}$  size each (full drift time 2200  $\mu\text{s}$ ). In each drift time bin, a Landau convolved with Gaussian function is fitted to the  $dQ/dx$  distribution (see Figure 8). The Landau function describes the signal charge distribution while the Gaussian function accounts for the effect of the electronics noise of the read-out system. Note that since the goal is to extract the peak value of the distribution, the fit range is restricted to the peak regions by scanning forward and backward in bin number from the most probable value (MPV) bin until the value of the bin (number of hits) has fallen below some threshold, typically 50% of the MPV. This technique improves accuracy and ensures that we are selecting more MIP-like signals. The  $\chi^2/\text{ndf}$  value of the Landau convolved Gaussian fit is required to be less than 5 to eliminate poor quality fits. After applying this criterion, the MPV of the fitted distribution in each bin is extracted and plotted as a function of average drift time (in  $\mu\text{s}$ ) as shown in Figure 7 (right). The amount of charge arriving at the anode ( $Q_A$ ) after a drift time  $t_{\text{drift}}$  to that leaving the cathode ( $Q_C$ ) can be extracted by fitting an appropriate functional form to this distribution.  $Q_C$  ( $Q_A$ ) is extracted by substituting  $t=0$  ( $t=2.2$  ms) in the functional form. For an exponential functional form, the ratio of  $Q_A/Q_C$  can be interpreted as an electron lifetime ( $\tau$ ) using the relation

$$\frac{Q_A}{Q_C} = \exp(-t_{\text{drift}}/\tau) \quad (1)$$

For non-exponential functional forms (exponential plus constant or polynomial of order 2 fits were used for some datasets), one cannot interpret  $Q_A/Q_C$  as an electron lifetime. For the example dataset shown in Figure 7 (right), the positive slope in the plot shows that there is more charge observed for longer drift times than at shorter drift times while one would expect more attenuation at longer drift times. This unexpected behavior resulting in  $Q_A/Q_C > 1$  is observed for a majority of the runs analyzed. It is interesting to note that the LongBo experiment [19] has also observed a similar scenario. A number of quantities were explored to understand this unexpected scenario. Among them, the most convincing explanation is provided by space charge.

### 6.1 Space charge in liquid argon

Space charge [17] refers to the build-up of slow-moving positive ions in the detector due primarily to ionization from cosmic rays, leading to a distortion of the electric field (both in direction and

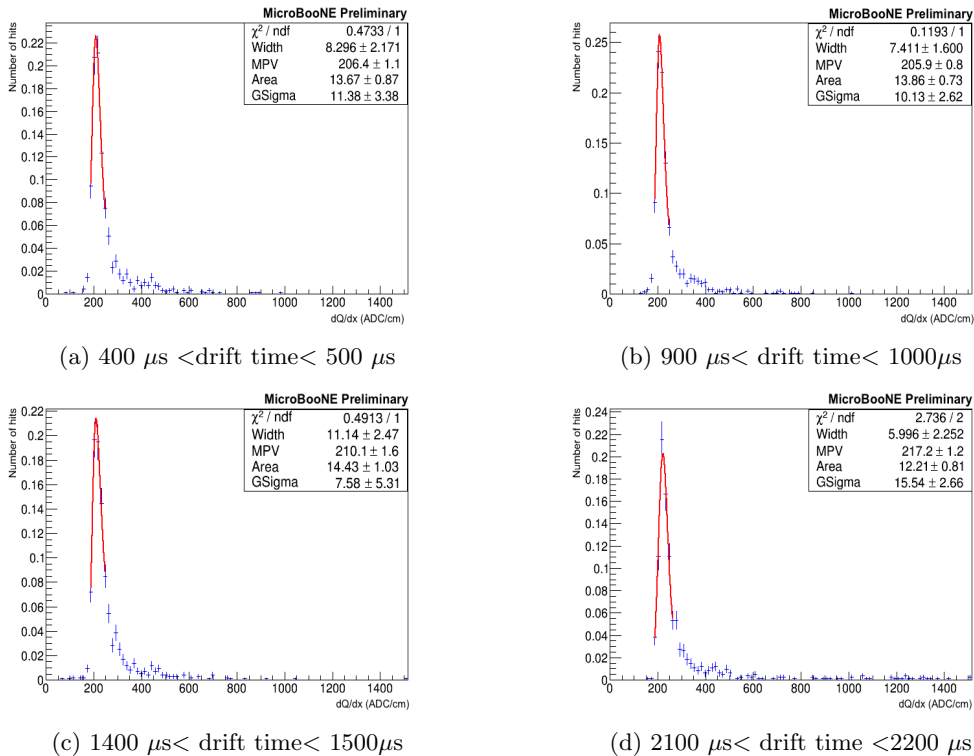


Figure 8: Figure illustrating Landau convolved Gaussian fits to the  $dQ/dx$  distributions in four drift bins for run 5411. Fits are restricted to the peak region to extract the most probable value (MPV) more accurately and improve the  $\chi^2/\text{ndf}$  of the fit.

magnitude) resulting in distortions in the reconstructed position of ionization electron clusters detected by the TPC wire planes. We will refer to this as “spatial SCE” where *SCE* stands for space charge effect. The presence of space charge also modifies the electron-ion recombination which is a function of electric field. We will refer to this as “recombination SCE”.

### 6.1.1 Effect of space charge on $dQ/dx$

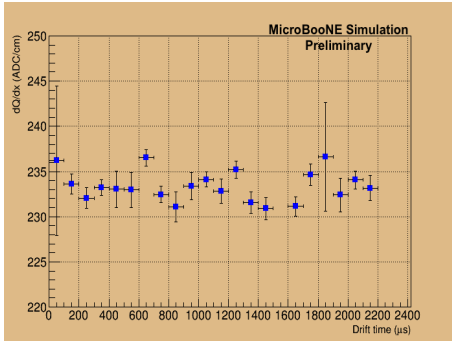
MicroBooNE is located near the earth’s surface with no overburden and the high influx of cosmic rays results in significant space charge effects [17] leading to both spatial and recombination SCE. Because the space charge varies over the volume of the TPC, the resulting electric field varies in direction and magnitude, affecting the drift trajectory and velocity. Following Ref. [17], the spatial SCE modifies the measured  $dQ/dx$  according to

$$(dQ/dx)_{\text{measured}} = 1.15 \times (dQ/dx)_{\text{true}} \times \cos(\alpha) \quad (2)$$

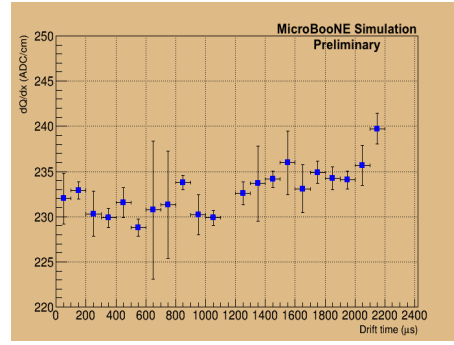
where  $\alpha$  is the angle of the track with respect to the wire planes. Reconstructed tracks with  $\alpha=90^\circ$  (perpendicular to the wire planes) will be minimally distorted whereas tracks with  $\alpha=0^\circ$  (parallel to the wire planes) will be most distorted. As an example, if the angle with respect to the cathode (or anode plane) for crossing tracks is  $45^\circ$ , one would expect about 8% increase in charge near the cathode.

The electric-field increases by 12% at the cathode and decreases by 5% at the anode due to space charge. The electron-ion recombination is a function of electric field and following the Modified-box model [16] is given by

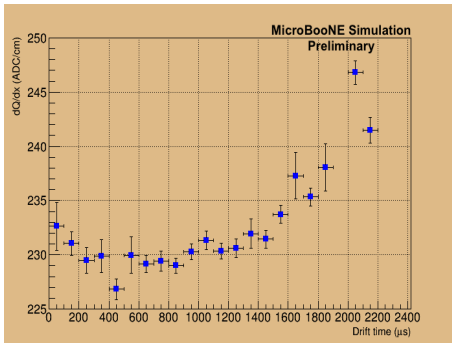
$$R_{\text{box}} = \frac{\ln\left(\alpha + \frac{\beta_p}{\rho\mathcal{E}} \cdot \frac{dE}{dx}\right)}{\frac{\beta_p}{\rho\mathcal{E}} \cdot \frac{dE}{dx}} \quad (3)$$



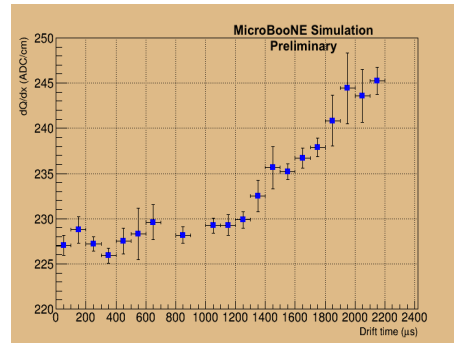
(a) Spatial SCE=off, Recombination SCE=off



(b) Spatial SCE=off, Recombination SCE=on



(c) Spatial SCE=on, Recombination SCE=off



(d) Spatial SCE=on, Recombination SCE=on

Figure 9:  $dQ/dx$  vs drift time curves for isotropic single muons with various space charge settings in simulation. The full event selection listed in Section 5 is applied including the shorted channels cut. Also, the electron lifetime is set to 1000 seconds and both longitudinal and transverse diffusion coefficients are set to zero to exclude any attenuation in  $dQ/dx$  caused by them.

where  $\mathcal{E}$  is the electric field (0.273 kV/cm for MicroBooNE),  $\rho$  is the liquid argon density (1.38 gm/cm<sup>3</sup> at a pressure of 18.0 psia), and parameters  $\beta_p=0.212\pm 0.002$  (kV/cm)(g/cm<sup>2</sup>)/MeV and  $\alpha=0.93\pm 0.02$ . The values for  $\alpha$  and  $\beta_p$  come from ArgoNeuT measurements [16] corresponding to an electric field of 0.481 kV/cm. Recombination is suppressed at higher fields and enhanced at lower electric fields. Two commonly used models of electron-ion recombination are the Birks model and the Modified-box model [16]. A feature of both of these models is that the recombination decreases with increasing electric field (because electrons drift faster in higher fields leaving less time to recombine). For MicroBooNE, the electric field is largest at the cathode, therefore more ionization electrons present, and thus a larger signal. A change in  $dQ/dx$  of  $-1.2\%$  ( $+3.55\%$ ) is expected at the anode (cathode) due to recombination SCE alone. The overall change in  $dQ/dx$  from cathode to anode is about 5%.

In order to study the unexpected  $Q_A/Q_C > 1$  phenomenon in simulation, a 3D space charge model is implemented. The default recombination model used in simulation is the modified box model [16]. In order to study effects due to space charge alone, other detector effects such as electron drift-lifetime and electron diffusion that can also produce attenuation in  $dQ/dx$  along the drift are turned off. Figure 9 shows the  $dQ/dx$  variation along the drift direction for isotropic single muons with and without space charge and recombination simulation. The positive slope in the plots indicates that the  $Q_A/Q_C > 1$  phenomenon arises mainly from space charge effects.

### 6.1.2 Space charge corrections

In order to correct for the space charge effect,  $dQ/dx$  corrections in each drift bin (for the 22 bins used in the analysis) are extracted using simulated samples. The space charge correction,  $C$ , is

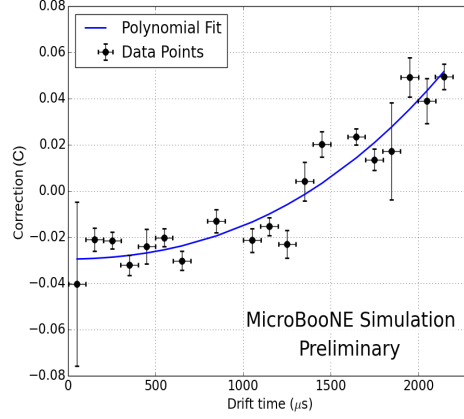


Figure 10: Space charge corrections with drift time fitted with a third order polynomial. Corrections,  $C$ , were extracted based on plots shown in Figure 9 and following Equation 4.

Drift bin ( $t$ )	Space Charge Correction ( $C'$ ) (%)
50 $\mu\text{s}$	-2.94
150 $\mu\text{s}$	-2.92
250 $\mu\text{s}$	-2.87
350 $\mu\text{s}$	-2.79
450 $\mu\text{s}$	-2.68
550 $\mu\text{s}$	-2.54
650 $\mu\text{s}$	-2.38
750 $\mu\text{s}$	-2.17
850 $\mu\text{s}$	-1.94
950 $\mu\text{s}$	-1.66
1050 $\mu\text{s}$	-1.35
1150 $\mu\text{s}$	-0.99
1250 $\mu\text{s}$	-0.59
1350 $\mu\text{s}$	-0.15
1450 $\mu\text{s}$	0.34
1550 $\mu\text{s}$	0.88
1650 $\mu\text{s}$	1.46
1750 $\mu\text{s}$	2.10
1850 $\mu\text{s}$	2.79
1950 $\mu\text{s}$	3.54
2050 $\mu\text{s}$	4.35
2150 $\mu\text{s}$	5.21

Table 2: Space charge  $dQ/dx$  corrections in the 22 drift bins obtained by comparing samples (a) and (d) of Figure 9 and using Eq. 4.

obtained using the formula,

$$C = \frac{\left(\frac{dQ}{dx}\right)_{(\text{SCE=on})} - \left(\frac{dQ}{dx}\right)_{(\text{SCE=off})}}{\left(\frac{dQ}{dx}\right)_{(\text{SCE=on})}} \quad (4)$$

Figure 9 shows the simulation samples used to extract the space charge corrections. Corrections were obtained by comparing samples (a) and (d) of Figure 9, where sample (d) includes both spatial and recombination SCE. The extracted corrections,  $C$ , are plotted as a function of drift time (Figure 10) and a polynomial of order three is fitted to the distribution. The final corrections,  $C'$ , for each drift bin are obtained from the fitted function and are shown in Table 2. Uncertainties associated to the space charge effect and extracted corrections are discussed in Section 8.1. The space charge corrections are applied to the data using

$$\left(\frac{dQ}{dx}\right)' = \frac{dQ}{dx}(1 - C') \quad (5)$$

where  $C'$  is listed in Table 2 and  $(dQ/dx)'$  stands for space charge corrected  $dQ/dx$ . As an example, Figure 11 shows the individual  $dQ/dx$  vs drift time plots for six data runs before (left) and after (right) applying the space charge corrections. Figure 12 shows a comparison of the  $Q_A/Q_C$  charge ratio over the data taking period 02/16/2016 to 04/21/2016 (as described in Section 3) with (black filled circles) and without (blue triangles) space charge corrections. After applying the corrections, all of the measured  $Q_A/Q_C$  values are consistent with being 1.0 or less within statistical errors.

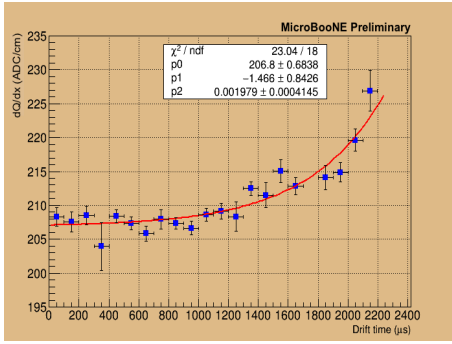
## 6.2 Comparison between Data and Simulation

The analysis method described in the previous section is validated using isotropic single-muon samples (as described in Section 3). We found that for simulated electron drift-lifetimes of up to 8 ms, the extracted drift-lifetime values are within an accuracy of 1% to 2% of the input drift-lifetimes.

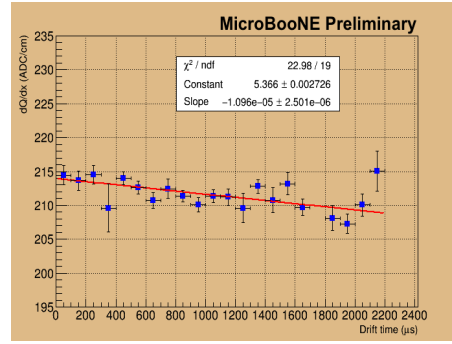
Since simulated samples are used to extract corrections (Section 6.1.2) and systematic uncertainties (Section 8) for the data, a comparison between data and simulation is performed. All the simulation samples used for comparison are isotropic single-muon samples (as defined in Section 3) which have different properties than cosmic-ray muons, for example, in terms of number of tracks per event and track angular distributions. However, since hits are treated independently from tracks in this analysis, a comparison at the hit level shows that we are sampling the same coordinate space as data. Figure 13 shows the hit  $X$ ,  $Y$ , and  $Z$  position comparison between data and simulation for all tracks with the shorted channels cut. All distributions are normalized to unity. For data, run 5910 is used with the full event selection applied. In the case of simulation, a single-muon isotropic sample is used with a electron drift-lifetime value of 1000 seconds. Simulated tracks with a minimum  $X$  projected length of 200 cm are used in the analysis along with all other selection cuts as data. Figure 13 shows that we are sampling the same coordinate space as data.

## 7 Location dependence of $Q_A/Q_C$

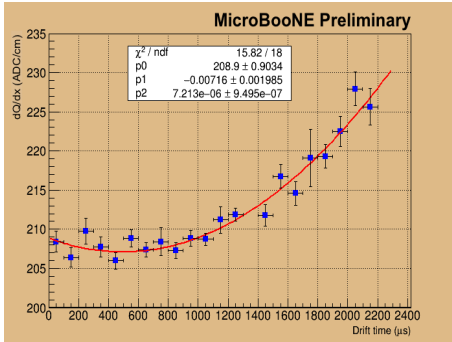
The motivation to look for variations of  $Q_A/Q_C$  transverse to the drift direction comes mainly from the fact that such variations were observed in other experiments, such as DUNE 35-ton prototype [20] and ICARUS [21]. The liquid argon purity was observed to vary along the vertical direction of these detectors. This observed non-uniformity mainly depends on the design of the argon recirculation system. For example, in the case of DUNE 35-ton prototype, the pump suction (where the liquid argon leaves the cryostat) was at the bottom as was the input (where the clean argon enters the cryostat). The circumstance that the incoming argon was cold and came in at the bottom of the cryostat and that the pump suction was also low in the tank meant that the clean argon did not circulate effectively throughout the cryostat resulting in the observed vertical dependence of electron drift-lifetime. Note that for both DUNE 35-ton prototype and ICARUS,



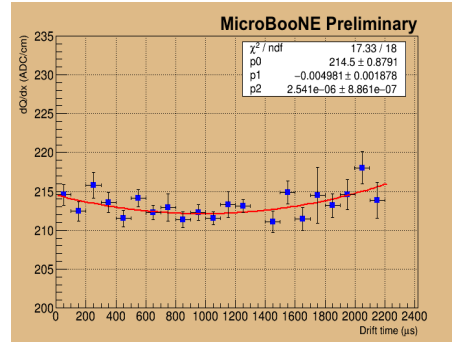
(a) 02/21/2016, day 6 (before),  
Exponential plus constant fit



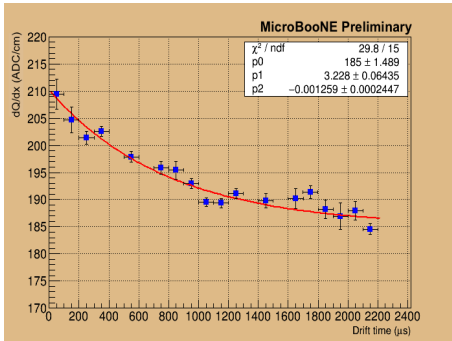
(b) 02/21/2016, day 6 (after),  
Exponential fit



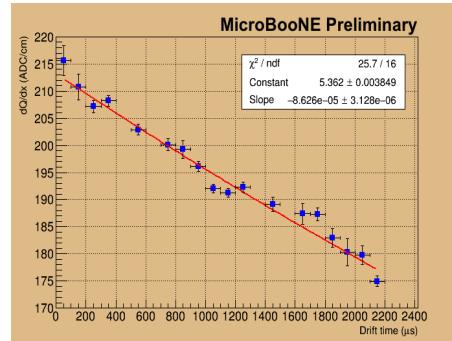
(c) 02/28/2016, day 13 (before),  
Polynomial of order 2 fit



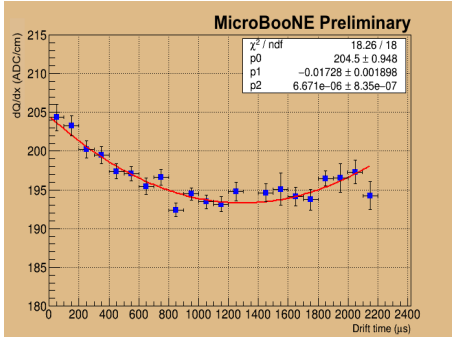
(d) 02/28/2016, day 13 (after),  
Polynomial of order 2 fit



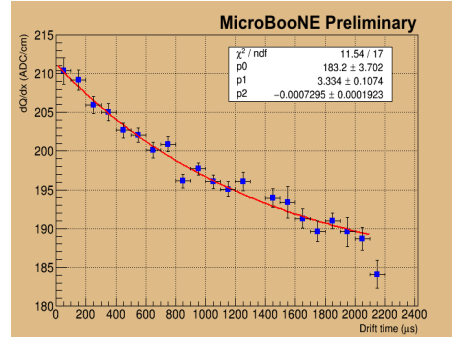
(e) 03/03/2016, day 17 (before),  
Exponential plus constant fit



(f) 03/03/2016, day 17 (after),  
Exponential fit



(g) 04/08/2016, day 43 (before),  
Polynomial of order 2 fit



(h) 04/08/2016, day 43 (after),  
Polynomial of order 2 fit

Figure 11:  $dQ/dx$  vs drift time plots for data before (left) and after (right) space charge corrections.

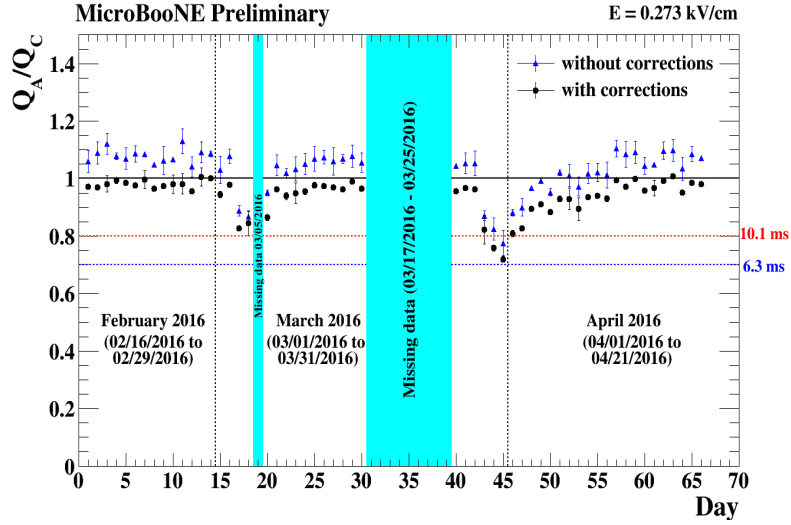


Figure 12: Variation of  $Q_A/Q_C$  over 56 days of data before (blue triangles) and after (black filled circles) applying space charge corrections. Error bars represent errors from the fitted function. The vertical cyan bands show missing data (see Section 3 for more details).

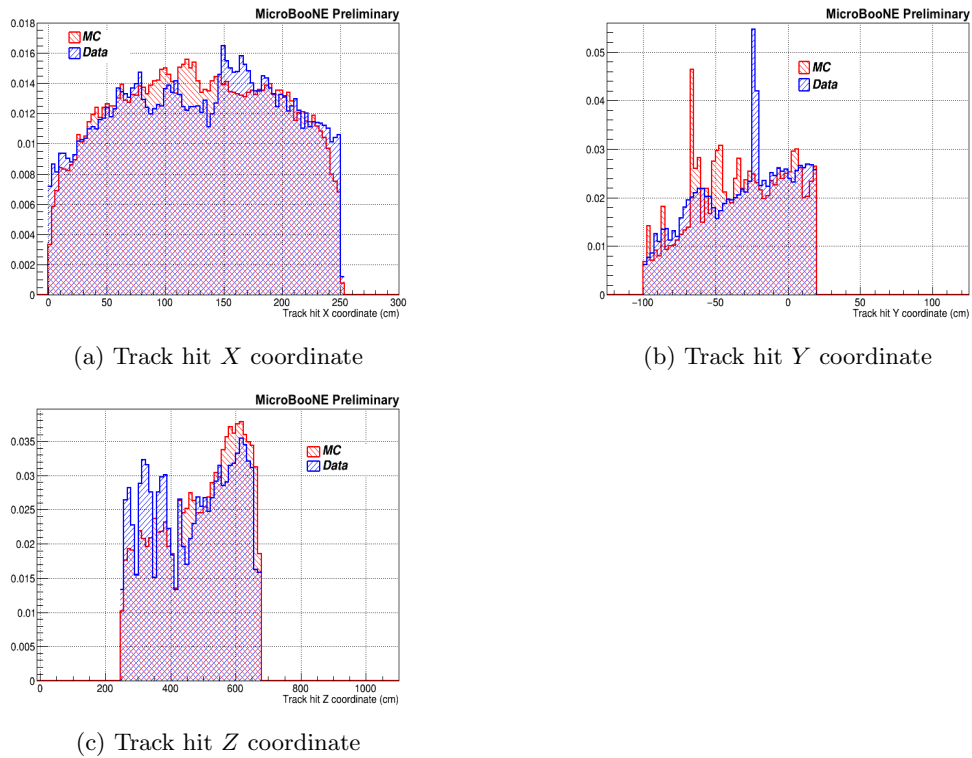


Figure 13: Comparison of track hit  $X$ ,  $Y$  and  $Z$  coordinates between data (run 5910) and isotropic single muons with the shorted channels cut. In the case of data, the drift ( $X$ ) coordinate is corrected for  $t_0$ . Both data and simulation are normalized to unity.

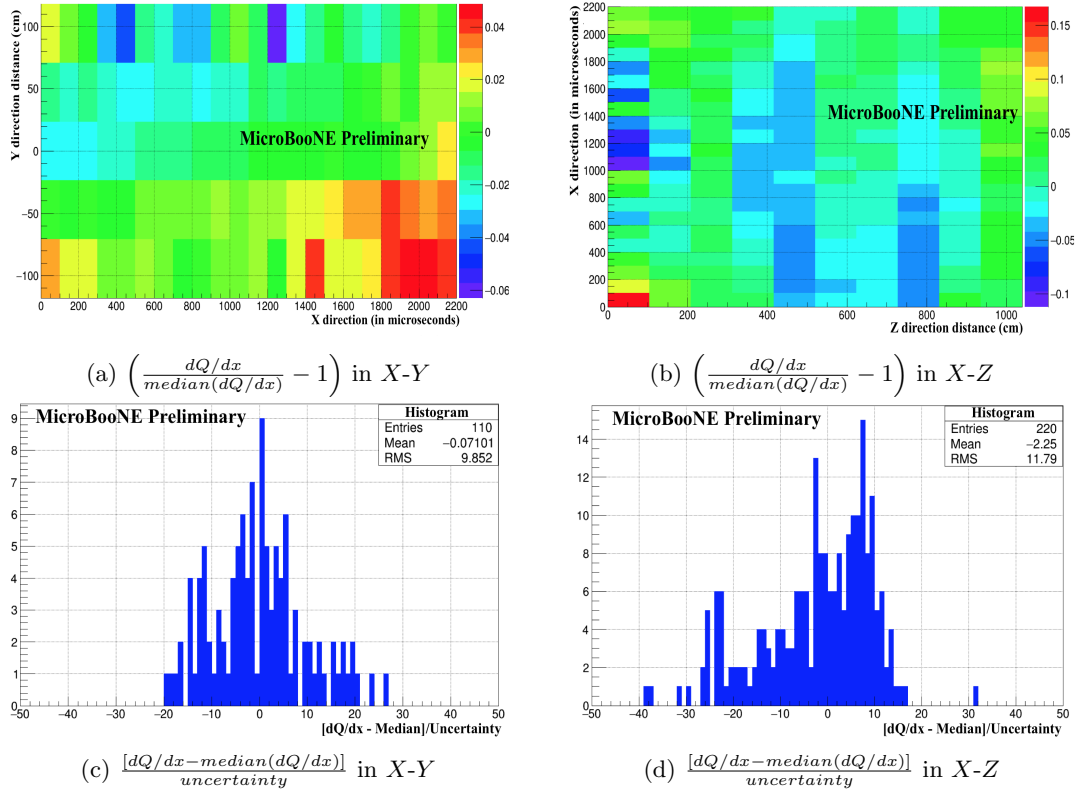


Figure 14: 2D and 1D representations of  $dQ/dx$  variation w.r.t. the median  $dQ/dx$  in top and bottom rows, respectively. Plots are made using a 100,000 event sample with out the shorted channels cut.

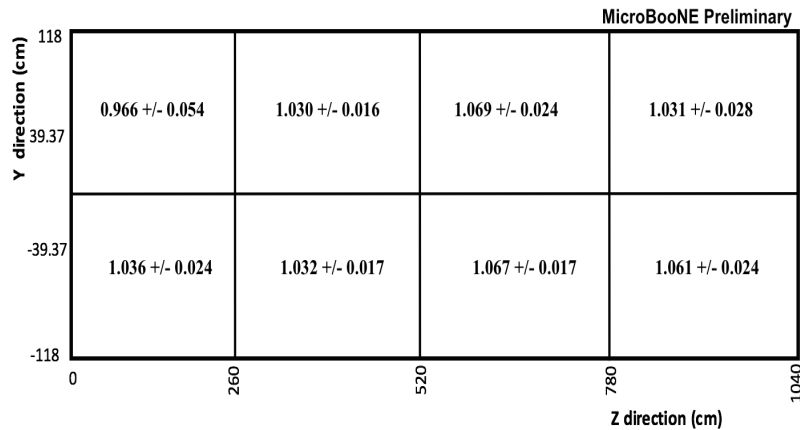


Figure 15: 2D map of  $Q_A/Q_C$  for non-drift ( $Y$  and  $Z$ ) directions using 100,000 cosmic-ray data events with the modified shorted channels cut but without space charge corrections.

when this dependence was observed, the electron lifetime was very low, around 3 ms and 2 ms, respectively, which made the effect more visible.

In the case of MicroBooNE (as described in Section 2), the pump suction is on the upstream end about seven inches from the bottom of the cryostat and the input of clean argon is on the downstream end right at the top of the liquid level. This is a significant difference compared to the experiments mentioned earlier. Because of this, MicroBooNE need not exhibit the same effects as the other experiments.

In order to estimate the location dependence of electron attenuation, a data-driven approach is used. As a first step, to illustrate how uniform our detector response is and how the combined magnitude of various effects such as space charge, recombination, lifetime, and wire-reponse uniformity affect the electron attenuation, the variation of  $dQ/dx$  across the detector is studied. The TPC is divided into ten (100 cm range) bins in the  $Z$  (beam) direction, five (50 cm range) bins in the  $Y$  (vertical) direction and twenty two drift time bins (100  $\mu$ s wide) along the  $X$  (drift) direction. In each  $X$ - $Z$  and  $Y$ - $Z$  bin, the most probable  $dQ/dx$  value is extracted using a Landau convolved Gaussian fit (same as the method described in Section 6). This analysis was performed without the shorted channels cut to study the  $dQ/dx$  variation throughout the TPC. Figure 14 (top row) shows the  $dQ/dx$  variation with respect to the median  $dQ/dx$  in  $X$ - $Y$  (left) and  $X$ - $Z$  (right) coordinate space. Figure 14 (bottom row) shows the 1D representations of the quantity shown in the top row for  $X$ - $Y$  (left) and  $X$ - $Z$  (right) coordinate space. From these plots, one can see that the  $dQ/dx$  varies by about 2 to 3% in the  $Y$  direction and about 2 to 5% in the  $Z$  direction.

To estimate the location dependence uncertainty, a 2D  $Q_A/Q_C$  map in  $Y$ - $Z$  is created by dividing the TPC into four bins, each with 260 cm range, along the  $Z$  direction and two bins, each with 118 cm range, along the  $Y$  direction. This binning is coarser compared to the binning used for studying the  $dQ/dx$  variation across the TPC (Figure 14). This is needed to obtain statistically adequate samples in each TPC sub-region. As we gain more statistics, a more finer binning can be used. In extracting the  $Q_A/Q_C$  values in each TPC bin, a 10 cm fiducial cut from all TPC boundaries is applied along with a modified version of the shorted channels cut as follows (note that these cuts are different from the shorted channel cuts described in Section 5):

- Exclude “Shorted  $U$ ” channel region:  $Z < 400$  cm and  $Y > [-120+Z/\tan(\pi/3)]$  cm and  $Y < [20+Z/\tan(\pi/3)]$  cm
- Exclude “Shorted  $W$ ” channel region:  $690$  cm  $< Z < 750$  cm
- Exclude “Misconfigured  $U$ ” channel region:  $Z > 800$  cm and  $Y < [-117+(Z-800)/\tan(\pi/3.0)]$  cm

Using this along with the event selection and analysis method described in Sections 5 and 6,  $Q_A/Q_C$  values are obtained in each TPC bin as shown in Figure 15. Note that the extracted  $Q_A/Q_C$  values are not corrected for space charge effect in order to minimize the impact of the large errors associated with the space charge corrections. Also, space charge effect is expected to be similar in the selected TPC sub-regions by the symmetry of the detector. The RMS spread of the  $Q_A/Q_C$  distribution from the 8 TPC sub-regions is calculated to be 3.3%. In order to ensure that the observed variation in  $Q_A/Q_C$  for various regions of the TPC is not arising from statistical fluctuations, a fit to the hypothesis that the  $Q_A/Q_C$  values are consistent with a common average is performed. This test yielded a  $\chi^2/\text{ndf}$  of 1.15 with  $\text{ndf}=7$  and  $(Q_A/Q_C)_{\text{average}} = 1.04$ . This shows that there is no evidence of location dependence of  $Q_A/Q_C$  in MicroBooNE and hence is not included in our final results.

## 8 Systematic uncertainties

A number of sources of systematic uncertainties are explored and presented here. While the list presented here may not be complete, we believe the most important systematics are addressed. Both data-driven and simulation based techniques are used to extract systematics such as those coming from space charge corrections, recombination model, and diffusion. A brief summary of

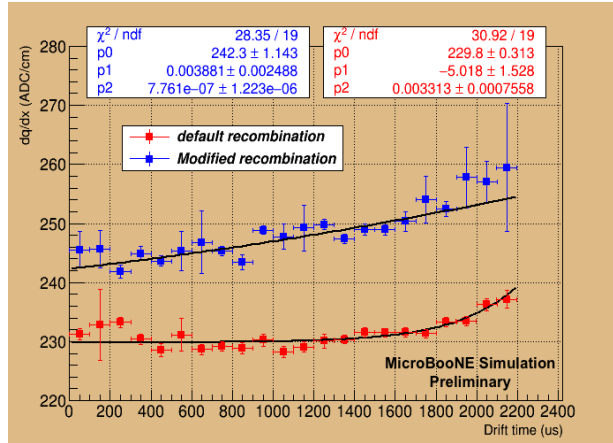


Figure 16: Variation in  $dQ/dx$  with drift time for isotropic single muons. The red points are the result of using the default modified box recombination model, and the blue points using the same model but with changed parameters. An exponential plus constant (polynomial of second order) fit to the default (modified) model is used.

other systematics not studied for this analysis that might effect  $dQ/dx$  but are expected to be small is presented in Section 10.

## 8.1 Space charge correction

The space charge correction is the single largest correction to the  $Q_A/Q_C$  ratio in this analysis. These preliminary corrections are extracted from the space charge models implemented [17] in the simulation that are currently only valid for the central region of the TPC. To account for this, we conservatively assign a large uncertainty associated to this correction by comparing the  $Q_A/Q_C$  values before and after the space charge correction and taking 50% of their difference as systematic uncertainty. This is done for all 56 datasets used in the analysis. The resulting systematic uncertainty on each of the  $Q_A/Q_C$  value is listed in Table 3. The uncertainty associated to space charge corrections ranges from 1.4% to 7.5% with an average uncertainty around 4.6%. This may be reduced after space charge models are fully constrained.

## 8.2 Recombination model

In the current default modified box model for recombination, the recombination effect is given by Eq. 3. In order to account for recombination model systematic uncertainties,  $\alpha$  and  $\beta_p$  in Eq. 3 are maximally varied by 0.1 and 0.01 (kV/cm)(g/cm<sup>2</sup>)/MeV, respectively. Two single-muon isotropic simulation samples were generated accordingly with only recombination SCE. Other effects such as electron drift-lifetime and electron diffusion that can alter  $dQ/dx$  were not included.

Figure 16 shows the  $dQ/dx$  variation with drift time. The red points are the result of using the default modified box model for recombination, and the blue points using the same model but with changed parameters to estimate the systematic uncertainty. The full event selection (including the shorted channels cut) and analysis method described in Sections 5 and 6 are applied. Using an exponential plus constant (polynomial of second order) fit to the default (modified) model as shown in the figure,  $Q_A/Q_C$  values are extracted for both cases. Although a shift in the  $dQ/dx$  values was observed between the two models, the overall variation of  $dQ/dx$  from cathode to anode, based on the fit, is small. A  $Q_A/Q_C$  value of  $1.042 \pm 0.032$  for the default model and  $1.052 \pm 0.039$  for the varied parameter model are calculated. The difference between the two values w.r.t. the default model value is 1.0% and is taken as the systematic error on recombination in our final result.

Day(s)	$Q_A/Q_C$ after space charge correction	Space charge correction uncertainty	Space charge correction uncertainty (%)
1	0.972	0.044	4.5
2	0.969	0.060	6.2
3	0.981	0.069	7.1
4	0.994	0.042	4.2
5	0.985	0.042	4.3
6	0.976	0.055	5.6
7	0.997	0.044	4.4
8	0.964	0.042	4.4
9	0.974	0.045	4.6
10	0.980	0.043	4.4
11	0.981	0.074	7.5
12	0.956	0.043	4.4
13	1.006	0.043	4.3
14	1.000	0.043	4.3
15	0.944	0.043	4.6
16	0.978	0.050	5.1
17	0.827	0.031	3.7
18	0.844	0.012	1.4
19	0.865	0.043	5.0
20	0.963	0.042	4.3
21	0.939	0.040	4.3
22	0.949	0.042	4.4
23	0.955	0.048	5.0
24	0.977	0.047	4.8
25	0.973	0.051	5.2
26	0.970	0.045	4.6
27	0.962	0.054	5.6
28	0.989	0.045	4.5
29	0.965	0.045	4.7
30	0.955	0.044	4.6
31	0.967	0.043	4.4
32	0.962	0.045	4.7
33	0.823	0.024	2.9
34	0.758	0.034	4.4
35	0.719	0.029	4.0
36	0.808	0.037	4.5
37	0.827	0.037	4.4
38	0.894	0.037	4.1
39	0.911	0.040	4.4
40	0.884	0.034	3.8
41	0.929	0.046	5.0
42	0.929	0.041	4.4
43	0.894	0.039	4.4
44	0.936	0.041	4.3
45	0.939	0.041	4.4
46	0.930	0.041	4.4
47	0.995	0.055	5.5
48	0.972	0.057	5.8
49	0.999	0.047	4.7
50	0.958	0.043	4.5
51	0.967	0.041	4.2
52	0.993	0.052	5.2
53	1.008	0.045	4.5
54	0.952	0.041	4.3
55	0.985	0.050	5.1
56	0.980	0.046	4.6

Table 3: Systematic uncertainties for space charge corrections on the  $Q_A/Q_C$  values for all 56 datasets.

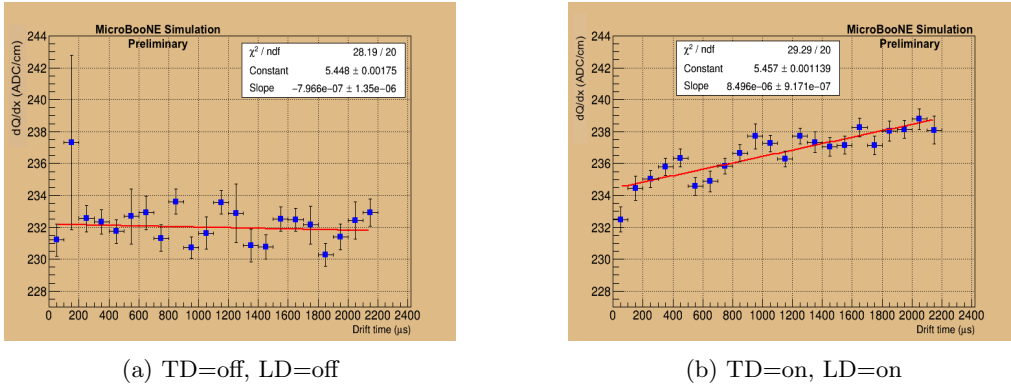


Figure 17:  $dQ/dx$  vs drift time distribution for isotropic single muons with (right) and without (left) diffusion. The electron lifetime is set to 1000 seconds and the space charge and recombination effects are turned off. The full event selection described in Section 5 is applied except for the shorted channels cut. TD here refers to transverse diffusion with a nominal value of  $16.2 \text{ cm}^2/\text{sec}$ . LD here refers to longitudinal diffusion with a nominal value of  $6.2 \text{ cm}^2/\text{sec}$ .

Systematic name	Uncertainty (%)
Space charge correction	5.0
Recombination model	1.0
Diffusion	2.0
Total	5.5

Table 4: Summary of systematic uncertainties in % on the final  $Q_A/Q_C$  value. In the case of space charge correction, the average uncertainty (from Table 3) is quoted. The total uncertainty is calculated by adding the individual uncertainties in quadrature.

### 8.3 Diffusion

Diffusion, especially transverse diffusion that is perpendicular to the drift direction, can smear the charge distribution arriving at the anode to neighboring wires, and affect the collected  $dQ/dx$ . In order to understand the effect of both longitudinal (along the drift direction) and transverse diffusion on electron attenuation, simulation samples with varied diffusion parameters are generated. Also, the effects from lifetime, space charge and recombination are turned off in order to study the effect solely coming from diffusion. Figure 17 shows the  $dQ/dx$  vs drift time curves with (right) and without (left) diffusion. Diffusion (mainly transverse component) modifies the lifetime in the same direction as does the space charge, but the effect is smaller. The  $Q_A/Q_C$  value is  $0.998 \pm 0.005$  ( $1.019 \pm 0.004$ ) for the sample without (with) diffusion. As an estimate of the systematic error from this effect, we use 100% of the  $Q_A/Q_C$  difference between the results with and without diffusion (2.0%).

### 8.4 Systematics summary

A summary of the systematic uncertainties calculated in this section is shown in Table 4. All the systematic uncertainties are added in quadrature to calculate the total systematic uncertainty which is then added in quadrature to the statistical errors corresponding to the space charge corrected  $Q_A/Q_C$  values (black points in Figure 12). These final uncertainties are applied to the space charge corrected  $Q_A/Q_C$  values to arrive at the final results.

## 9 Results

Figure 18 shows the variation in  $Q_A/Q_C$  as a function of time with both systematic and statistical uncertainties. It can be seen that even with systematic errors the purity of liquid argon throughout the data period considered is very high during stable purity conditions with  $Q_A/Q_C$  values ranging

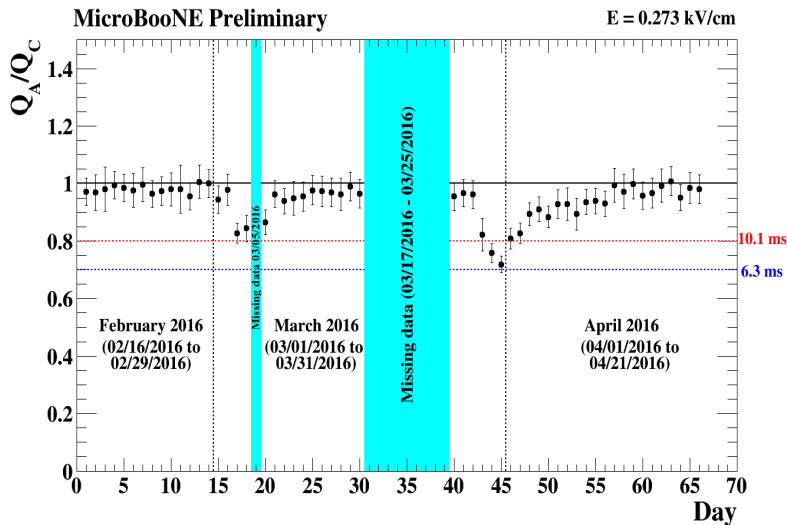


Figure 18: Variation in  $Q_A/Q_C$  as a function of time after space charge corrections and including both statistical and systematic uncertainties. The uncertainties are dominated by systematics, and are expected to be largely correlated among all the points. The vertical cyan bands show missing data as explained in Section 3.

from  $0.88 \pm 0.04$  to  $1.01 \pm 0.05$ . Following Eq. 1 and using the full drift time for our TPC (2.2 ms to drift from cathode to anode), the lowest  $Q_A/Q_C$  charge ratio ( $0.88 \pm 0.04$ ) observed during stable purity period results in an electron drift-lifetime of 18.0 ms. This corresponds to a charge loss of 12% crossing the entire TPC at our nominal electric field of 0.273 kV/cm and an  $O_2$  equivalent contamination of 17 ppt. The low purity regions also show relatively high  $Q_A/Q_C$  ratios, ranging from  $0.72 \pm 0.03$  to  $0.87 \pm 0.04$ . The lowest  $Q_A/Q_C$  ratio ( $0.72 \pm 0.03$ ) over the entire data period analyzed corresponds to 6.8 ms which corresponds to a charge loss of 28%, over the full drift, at our nominal field and an  $O_2$  equivalent contamination of 44 ppt.

## 10 Future plans

There are other effects in the detector that might impact the extracted  $dQ/dx$  which are not currently accounted for. One comes from the induced charge on a given wire from electrons drifting to nearby wires. Here, the electrons drifting to wires near the target wire also induce charge on the target wire. However this is expected to be a small effect for the collection plane which is what is used in the analysis. Also, the  $2 \mu\text{s}$  electronics shaping time is expected to further reduce this effect. Another effect that is currently not considered for this analysis is the variation in the gain and shaping time of the electronics and how it affects the charge collection. Although a  $2 \mu\text{s}$  shaping time is used in processing the signal at MicroBooNE, the actual shaping time of the electronics varies by about 2.5% across the detector. We plan to incorporate these in a future iteration of the analysis.

Another concern is that the space charge, recombination and diffusion corrections and related uncertainties are extracted from models implemented in simulation. In the case of recombination and diffusion, the effect is expected to be small as demonstrated in Sections 8.2 and 8.3, respectively. In the case of space charge, as discussed in Section 6.1.1, the effects modeled in simulation correspond to the central Y/Z region of the TPC where the effects are expected to be maximal. Hence one can consider the modeled effects as the worst case scenario. MicroBooNE is anticipating results on space charge, recombination and diffusion measurements using TPC information in the near future and we plan to incorporate them in a future iteration of this analysis. Furthermore, a complete calibration of the space charge effect throughout the entire active TPC volume by utilizing a recently installed larger cosmic ray tagger system and/or a UV laser calibration system [8, 22] is planned for the future.

## 11 Summary and conclusions

We report first measurements of liquid-argon purity in MicroBooNE expressed in terms of the ratio of collected charge to deposited charge,  $Q_A/Q_C$ , using cosmic-ray muons. Analysis of the runs during the time period, 02/16/2016–04/21/2016, show that the purity of liquid argon is very high, with  $Q_A/Q_C$  values ranging from  $0.72\pm 0.03$  to  $1.01\pm 0.05$ . Systematic uncertainties dominate the measurement. The lowest electron drift-lifetime observed over the full data period analyzed is 6.8 ms corresponding to an O<sub>2</sub> equivalent contamination of 44 ppt and a charge loss of 28%, at full drift and nominal electric field. During stable purity period, the lowest electron drift-lifetime observed is 18.0 ms which corresponds to a charge loss of 12%, over the full drift distance, at our nominal field and an O<sub>2</sub> equivalent contamination of 17 ppt. This is an indication that the argon purification and recirculation system of MicroBooNE is performing very well, substantially exceeding the MicroBooNE design goal of 3-ms electron drift-lifetime.

## References

- [1] E. Buckley *et al.*, “A study of ionization electrons drifting over large distances in liquid argon”, Nucl. Instrum. and Methods in Physics Research A 275, 364-372 (1989).
- [2] A. Bettini *et al.*, “A study of the factors affecting the electron lifetime in ultra-pure liquid argon”, Nucl. Instrum. and Methods in Physics Research A 305, 177-186 (1991).
- [3] The MicroBooNE Collaboration, “Measurement of the Electronegative Contaminants and Drift Electron Lifetime in the MicroBooNE Experiment”, MICROBOONE-NOTE-1003-PUB (2016).
- [4] S. Amoruso *et al.*, “Analysis of the liquid argon purity in the ICARUS T600 TPC”, Nucl. Instrum. and Methods in Physics Research A 516, 68–79 (2014).
- [5] A. Ereditato *et al.*, “Design and operation of ARGONTUBE: a 5 m long drift liquid argon TPC”, JINST 8, P07002 (2013).
- [6] M. Antonello *et al.*, “Experimental observation of an extremely high electron lifetime with the ICARUS-T600 LAr-TPC”, JINST 9, P12006 (2014).
- [7] The MicroBooNE Collaboration, *Technical Design Report*, <http://www-microboone.fnal.gov/publications/TDRCD3.pdf> (2011).
- [8] The MicroBooNE Collaboration, “Design and construction of the MicroBooNE detector”, JINST 12, P02017 (2017).
- [9] A. A. Aguilar-Arevalo *et al.*, “Unexplained Excess of Electron-like Events from a 1 GeV Neutrino Beam”, Phys. Rev. Lett. 102, 101802 (2009).
- [10] A. A. Aguilar-Arevalo *et al.*, “A Combined  $\nu_\mu \rightarrow \nu_e$  and  $\bar{\nu}_\mu \rightarrow \bar{\nu}_e$  Oscillation Analysis of the MiniBooNE Excesses”, Phys. Rev. Lett. 110, 161801 (2013).
- [11] Sigma-Aldrich, P.O. Box 14508, St. Louis, MO 63178 USA.
- [12] BASF Corp., 100 Park Avenue, Florham Park, NJ 07932 USA.
- [13] E. D. Church, “Larsoft: A software package for liquid argon time projection drift chambers”, arXiv:1311.6774 (2016).
- [14] The MicroBooNE Collaboration, “Noise Characterization and Filtering in the MicroBooNE Liquid Argon TPC”, JINST 12, P08003 (2017).
- [15] The ArgoNeuT Collaboration, “Analysis of a large sample of neutrino-induced muons with the ArgoNeuT detector”, JINST 7, P10020 (2012).

- [16] The ArgoNeuT Collaboration, “A study of electron recombination using highly ionizing particles in the ArgoNeuT Liquid Argon TPC”, JINST 8, P08005 (2013).
- [17] The MicroBooNE Collaboration, “Study of space charge effects in MicroBooNE”, MICROBOONE-NOTE-1018-PUB (2016).
- [18] Convolved Landau and Gaussian Fitting Function,  
<https://root.cern.ch/root/html/tutorials/fit/langaus.C.html>
- [19] The LongBo Collaboration, “Design and operation of LongBo: a 2 m long drift liquid argon TPC”, JINST 10, P07015 (2015).
- [20] The DUNE 35-ton Prototype Collaboration, “Evidence of Impurity Stratification in the DUNE 35 ton Prototype Cryostat”, FERMILAB-TM-2642-ND (2017).
- [21] The ICARUS Collaboration, “Measurement of the  $\mu$  decay spectrum with the ICARUS liquid Argon TPC”, Eur. Phys. J. C 33, 233 (2004).
- [22] A. Ereditato *et al.*, “A steerable UV laser system for the calibration of liquid argon time projection chambers”, JINST 9, T11007 (2014).